

Inverse design of flat-foldable thick origami with smooth curved surface

Byoung-Gyu Kim¹, Geon Hee Cho¹, Hak-Tae Lee², and Jinkyu Yang¹

¹Department of Mechanical Engineering, Seoul National University, 1 Gwanak-ro, Gwanak-gu, Seoul 08826, South Korea

²Department of Aerospace Engineering and the Program in Aerospace Systems Convergence, Inha University, 100 Inha-ro, Michuhol-gu, Incheon 22212, South Korea

Abstract

Origami as a deployable structure offers the unique advantage of achieving compact stowage via flat-folding while forming a well-defined surface composed of rigid panels upon deployment. However, since origami consists of flat facets, it is inherently limited in forming smooth curved surfaces upon deployment. This limitation restricts its applicability in systems where smooth curved geometries are essential for performance, such as aerospace systems and electromagnetic communication devices. Herein, we propose an inverse design methodology for thick origami that is capable of flat-folding while forming a smooth curved outer surface upon deployment. By establishing flat-foldable constraints that specify the positions of the creases, our method constructs thick origami capable of flat-folding even with panels that include a curved facet. Furthermore, by representing the origami layout as a graph, we enumerate all possible origami configurations and enable flexible design of the internal structure. Analytical results show that the optimized packaging ratio increases as the number of cells in a layout increases, indicating that the proposed design methodology provides controllability over the packaging ratio through the number of cells. Using our proposed design methodology, we fabricated a deployable origami wing and demonstrated its functionality through successful flight testing, in which the wing was subjected to aerodynamic loads. Our work proposes a new strategy for packaging smooth curved surfaces, addressing the packaging challenges encountered in aerospace and electromagnetic communications and thereby providing greater design freedom.

1 Introduction

Origami, an ancient art of paper folding, has emerged as a powerful design paradigm in diverse fields such as metamaterials [1–5], robotics [6–8], space exploration [12, 13], and deployable structures [9–11], owing to its unique geometry and reconfigurable nature. In particular, origami-based deployable structures exhibit the unique capability of achieving highly compact packaging via flat-folding, while maintaining minimal or no facet deformation during deployment. Unlike bar-linkage mechanisms [14, 15] that cannot form continuous deployed surfaces or inflatable membranes [16, 17] that rely on constant pressure to maintain their shape, origami-based deployable structures can be compactly stowed and, once deployed, form self-supporting configurations with continuous, well-defined surfaces.

Despite their unique advantages, origami-based deployable structures, composed of flat panels, are fundamentally limited in their applicability to curved geometries. Therefore, origami-based deployable structures have difficulty addressing stowage problems that involve curvature—for example, accommodating the wings of a Mars aerial explorer [18, 19] or packaging an antenna [20] within the limited payload volume of a rocket fairing.

In recent years, considerable efforts have been made to design origami structures capable of approximating or matching curved surfaces upon deployment, using diverse origami patterns such as Miura-ori [21–24], Resch [25, 26], and flasher [27–29], as well as thick origami [30, 31]. In most of these studies, the deployed surface appears bumpy rather than smooth, as it consists of flat panels that only discretely approximate the target curvature. This bumpy surface limits their applicability in systems that require smooth continuous curvature for optimal aerodynamic or electromagnetic performance, such as aircraft wings or reflector antennas. Some studies [28, 30] have achieved smooth curved surfaces upon deployment, but their applicability is limited to specific geometries, such as parabolic surfaces.

In this work, we introduce an inverse design methodology that enables the construction of deployable 3D thick origami structures with smooth curved outer surfaces tailored to a given target geometry. The method can be applied to all developable surfaces that can be classified as generalized cylinders or generalized cones. Our method first enumerates origami layouts using a planar graph representation, and then converts them into flat-foldable thick origami structures with smooth curved outer surfaces through a geometric construction guided by the flat-foldable constraints we define. We further analyze the relationship between the optimized packaging ratio and the number of origami cells, revealing that the packaging efficiency varies depending on the target shape. We demonstrated the versatility of our methodology by converting various generalized cylinders and generalized cones into flat-foldable thick origami structures (Fig. 3). Furthermore, we designed and fabricated a deployable aircraft wing using our method (Fig. 5), and a successful flight test demonstrated its robust applicability to practical engineering systems.

2 Results

2.1 Inverse design of flat-foldable thick origami for generalized cylinders

To begin with, the origami layout—defined by the connectivity among panels—is represented as a planar graph, as illustrated in Fig. 1a, and all allowable layouts were generated through canonical augmentation (Supplementary Note 1). Next, as shown in the center of Fig. 1a, one of the generated origami layouts is selected and embedded onto the cross-section of the target shape, which determines the approximate configuration of the overall origami structure. However, the embedded origami layout does not provide the exact geometry of the origami, such as the precise panel shapes or crease locations. Accordingly, based on the origami layout embedding, we generated the exact geometry of a flat-foldable thick origami with a smooth outer curved surface, as illustrated in Fig. 1b–d.

To construct flat-foldable thick origami for generalized cylinders, we define a generalized cylinder as the extrusion of an arbitrary closed curve along a specified direction vector \mathbf{e} (left of Fig. 1a) [33]. $\mathbf{f}(s)$ denotes the closed curve obtained from the intersection of the generalized cylinder with the plane orthogonal to \mathbf{e} , which we assume to coincide with the xy -plane for simplicity. This allows us to define the three-dimensional geometry of the origami structure through its two-dimensional geometry on the xy -plane, since the generalized cylinder is defined as an extrusion along the direction vector \mathbf{e} .

Next, as illustrated in Fig. 1b, each internal face of the embedded origami layout is converted into a flat-foldable thick origami that possesses a curved surface, which we refer to as a thick origami cell. First, as shown in the first and second stages of Fig. 1b, by offsetting the edges adjacent to \mathbf{q}_1 , we simultaneously generate the panels and determine the locations of the creases \mathbf{q}'_2 and \mathbf{q}'_4 . Here, the positions of \mathbf{q}'_2 and \mathbf{q}'_4 are determined by the two equations below, which ensure that the two panels adjacent to \mathbf{q}'_2 have equal thicknesses and, likewise, the two panels adjacent to \mathbf{q}'_4 have equal thicknesses.

$$\max_{s_3 \leq s \leq s'_2} \frac{-\det[\mathbf{f}(s) - \mathbf{q}_3 \quad \mathbf{q}'_2 - \mathbf{q}_3]}{\|\mathbf{q}'_2 - \mathbf{q}_3\|} = \frac{-\det[\mathbf{q}'_2 - \mathbf{q}_1 \quad \mathbf{q}_2 - \mathbf{q}_1]}{\|\mathbf{q}_2 - \mathbf{q}_1\|} \quad (1)$$

$$\max_{s'_4 \leq s \leq s_3} \frac{\det[\mathbf{f}(s) - \mathbf{q}_3 \quad \mathbf{q}'_4 - \mathbf{q}_3]}{\|\mathbf{q}'_4 - \mathbf{q}_3\|} = \frac{\det[\mathbf{q}'_4 - \mathbf{q}_1 \quad \mathbf{q}_4 - \mathbf{q}_1]}{\|\mathbf{q}_4 - \mathbf{q}_1\|} \quad (2)$$

By imposing equal thickness for the panels adjacent to each crease, we ensure that the thick origami cells can stack without interference when flat-folded, as shown in Fig. 1d. Subsequently, as shown in the third stage of Fig. 1b, we perform an additional inward offset by t_1 and t_2 , respectively. The creases \mathbf{v}_1 and \mathbf{v}_3 are determined as the intersection points of the offset lines, and the values of t_1 and t_2 are chosen to satisfy equation (3), which ensures that the distances between \mathbf{v}_1 and \mathbf{v}_3 , measured on the two panels adjacent to \mathbf{q}'_2 and \mathbf{q}'_4 , respectively, are equal when the creases \mathbf{q}'_2 and \mathbf{q}'_4 are fully unfolded (folding angle = 180°).

$$\|\mathbf{R}(\mathbf{e}, \phi_{\mathbf{q}'_2})(\mathbf{v}_3 - \mathbf{q}'_2) + \mathbf{q}'_2 - \mathbf{v}_1\| = \|\mathbf{R}(-\mathbf{e}, \phi_{\mathbf{q}'_4})(\mathbf{v}_3 - \mathbf{q}'_4) + \mathbf{q}'_4 - \mathbf{v}_1\| \quad (3)$$

In equation (3), $\mathbf{R}(\mathbf{e}, \phi_{\mathbf{q}'_2})$ denotes the Rodrigues' rotation matrix with \mathbf{e} as the rotation axis and $\phi_{\mathbf{q}'_2}$ as the rotation angle. This constraint ensures that the creases can fully fold or unfold without deformation, allowing the thick origami cells to achieve flat-folding, as illustrated in Fig. 1d. In this flat-folded state, all internal faces become coplanar, eliminating the internal volume and thereby significantly reducing the overall volume of the structure. Further details on the flat-foldable constraints and the thick origami

geometry are provided in Supplementary Note 2. Finally, as shown in the last stage of Fig. 1b and in Fig. 1c, the geometry defined in the plane is extruded along the extrusion vector \mathbf{e} , generating the thick origami cell and its corresponding crease lines.

The complete thick origami structure is obtained, as shown in Fig. 1d, by assembling the flat-foldable thick origami cells through bonding along the internal edges of the embedded graph. However, one internal edge incident to each internal vertex is left unbonded. This unbonded edge provides the necessary degree of freedom for the entire structure to fold. In contrast, if the unbonded edge is mechanically secured, the folding motion is restricted, which locks the deployed state (see Supplementary Note 2 for details).

Since our methodology is independent of the cross-sectional shape of a generalized cylinder, it can be applied to a broad range of geometries. As shown in Fig. 3a,b, our method can be applied to a variety of geometric shapes. Further, our methodology can also be applied to engineeringly relevant shapes such as aircraft wings (Fig. 5). It can be applied to diverse airfoil profiles, and with appropriate graph embedding, the deployed state can be designed to include internal structures such as spars.

2.2 Inverse design of flat-foldable thick origami for generalized cones

By extending the approach established for generalized cylinders, we also address generalized cones, which intrinsically require a 3D geometric description of thick origami. First, we define a generalized cone as the surface obtained by linearly expanding an arbitrary two-dimensional closed curve from an apex specified by the vector \mathbf{o} , as shown on the left of Fig. 2a [33]. In the case of a generalized cone, the origami layout is embedded on the spherical cross-section obtained by intersecting the generalized cone with the unit sphere centered at the apex \mathbf{o} , as shown in the middle of Fig. 2a. Moreover, we represent the geometry of the origami structure on the spherical cross-section in the form of a spherical figure, and radially extrude it to construct the entire geometry, as shown on the right of Fig. 2a. This allows the 3D geometry of the thick origami structure to be fully defined on a 2D spherical surface, thereby simplifying the overall design process. Specifically, all possible creases pass through the apex \mathbf{o} and are perpendicular to the spherical surface, ensuring that each panel defined as the spherical figure remains confined to the spherical cross-section even after rotations induced by folding.

As in the case of the generalized cylinder, each internal face of the origami layout embedded on the spherical cross-section is converted into a thick origami cell with a smooth outer curved surface, as shown in Fig. 2b. To make the thick origami flat-foldable, we transform the flat-foldable constraints defined on the plane (equations (1)–(3)) into their spherical-geometric form. First, the positions of the creases \mathbf{p}'_2 and \mathbf{p}'_4 , which correspond to the creases \mathbf{q}'_2 and \mathbf{q}'_4 in the generalized cylinder case, are determined by the following two equations.

$$\min_{s_3 \leq s \leq s'_2} \mathbf{R}(\mathbf{p}'_2, \phi_{\mathbf{q}'_2}) \mathbf{g}(s) \cdot (\mathbf{p}_1 \times \mathbf{p}_2) = 0 \quad (4)$$

$$\min_{s'_4 \leq s \leq s_3} \mathbf{R}(-\mathbf{p}'_4, \phi_{\mathbf{q}'_4}) \mathbf{g}(s) \cdot (\mathbf{p}_4 \times \mathbf{p}_1) = 0 \quad (5)$$

Note that all vectors originate from the apex \mathbf{o} with unit length, and the curve $\mathbf{g}(s)$ represents the closed intersection between the generalized cone and the unit sphere centered at \mathbf{o} . Equations (4) and (5) are the spherical-geometric counterparts of equations (1) and (2). They enforce equal thickness, measured as spherical distances, for the panels adjacent to \mathbf{p}'_2 and \mathbf{p}'_4 , respectively. As shown in Fig. 2c, this constraint prevents interference in the flat-folded state. The positions of the creases \mathbf{u}_1 and \mathbf{u}_3 , which correspond to the creases \mathbf{v}_1 and \mathbf{v}_3 in the generalized cylinder case, are determined such that they satisfy the following equation.

$$\mathbf{R}(\mathbf{p}'_2, \phi_{\mathbf{q}'_2}) \mathbf{u}_3 \cdot \mathbf{u}_1 = \mathbf{R}(-\mathbf{p}'_4, \phi_{\mathbf{q}'_4}) \mathbf{u}_3 \cdot \mathbf{u}_1 \quad (6)$$

Equation (6) is the spherical-geometric counterpart of equation (3), obtained by replacing the straight-line distance between the corresponding creases with the spherical distance. This constraint ensures that the creases can fully fold or unfold without deformation, allowing the thick origami cells to achieve flat-folding.

All vectors originate from the apex \mathbf{o} and have unit length. The curve $\mathbf{g}(s)$ represents the closed intersection between the generalized cone and the unit sphere centered at \mathbf{o} . Further details on the flat-foldable constraints and the thick origami geometry are provided in Supplementary Note 3.

As shown in Fig. 2c, the entire thick origami structure is constructed in the same manner as the generalized cylinder case—by bonding the flat-foldable thick origami cells along the internal edges of

the embedded graph. One internal edge incident to each internal vertex remains unbonded, providing the necessary degree of freedom for folding. As in the generalized cylinder case, mechanically securing this unbonded edge restricts the folding motion and locks the deployed configuration (see Supplementary Note 3 for details).

As in the generalized cylinder case, the method for the generalized cone is independent of the cross-sectional shape, and can therefore be applied to various geometries, as demonstrated in Fig. 3c,d. In addition, it can be applied to engineeringly useful geometries such as tapered wings and conical spiral antennas.

2.3 Relationship between packaging ratio and layout cell count

For both the generalized cylinder and generalized cone cases, we designed thick origami structures to be flat-foldable for compact stowage. We quantitatively evaluated how compactly the structure can be stowed using the packaging ratio η , defined as $\eta = \frac{V}{v}$, where V and v denote the volumes of the target shape and the flat-folded configuration, respectively. The packaging ratio η is determined by the geometry of the thick origami, and, as shown in Supplementary Notes 2 and 3, the geometry of the thick origami is determined by the embedding of the origami layout. Therefore, given a target shape and an origami layout, a maximally compact flat-folded configuration can be obtained by optimizing the vertex positions of the origami layout to maximize the packaging ratio. Furthermore, as shown in Fig. 4a, the origami layout—particularly the number of cells—also affects the optimized packaging ratio. In Fig. 4a, the packaging ratio increases from 4.2 to 6.4 as the number of cells used increases from 4 to 6. Therefore, we conducted an analysis to investigate how the optimized packaging ratio varies with the number of cells in the origami layout.

First, we restrict the target shape to a generalized cylinder with a convex and differentiable cross-section (i.e., the closed curve formed by $\mathbf{f}(s)$ is convex and smooth). This allows the packaging ratio η to be expressed as $\eta = \frac{A}{a}$, where A and a denote the cross-sectional areas of the target shape and the flat-folded configuration, respectively (see Supplementary Note 4). Furthermore, when all central angles $\Delta\theta_i$ defined for the cells in Fig. 4b are sufficiently small, the flat-foldable constraints can be approximately applied through a series expansion, allowing the packaging ratio η to be expressed as follows.

$$\eta = \frac{A}{\sum_i \frac{1}{16} r_i |\kappa_i| \left(r_i^2 + 2r'(\theta_i)^2 \right) \Delta\theta_i^2} \quad (7)$$

Here, $r(\theta)$ is defined in Fig. 4b, and $r_i = r(\theta_i)$, $r'(\theta_i) = \left. \frac{dr}{d\theta} \right|_{\theta=\theta_i}$, and κ denotes the curvature, with $\kappa_i = \kappa(\theta_i)$. Note that the origami layout is assumed to have a single internal vertex, and t_1 and t_2 are set to zero. The detailed derivation is provided in Supplementary Note 4. In the continuum limit, where all $\Delta\theta_i$ approach zero (i.e., when the number of cells n is very large), the optimized packaging ratio η_{opt} can be derived by applying the Cauchy–Schwarz inequality to equation (7) as follows:

$$\eta_{\text{opt}} = \frac{A}{\left(\int_0^{2\pi} \sqrt{\frac{1}{16} r(\theta) |\kappa(\theta)| \left(r(\theta)^2 + 2r'(\theta)^2 \right)} d\theta \right)^2} \cdot n \quad (8)$$

In this expression, n denotes the number of cells. In the continuum limit, equation (8) gives the attainable upper bound of η imposed by the Cauchy–Schwarz inequality; therefore, equation (8) corresponds to the global maximum of the packaging ratio in the continuum limit. According to the equality condition of the Cauchy–Schwarz inequality, the packaging ratio η reaches the global maximum in the continuum limit (equation (8)) when $a_1 = a_2 = \dots = a_i = \dots = a_n$, where a_i denotes the cross-sectional area of the i th cell in the flat-folded configuration. The upper plot of Fig. 4c shows the results for target shapes of elliptic cylinders with various eccentricities, illustrating equation (8) (solid lines) and the local maxima of the packaging ratio obtained from numerical optimization (markers). Even when the number of cells is not sufficiently large, we were able to find local maxima of the packaging ratio that follow the trend predicted by equation (8). As shown in the lower plot of Fig. 4c, the coefficient of variation of $\{a_1, a_2, \dots, a_i, \dots, a_n\}$ at the corresponding local maxima in the upper plot of Fig. 4c decreases as the number of cells increases (i.e., as the origami layout approaches the continuum limit). This result agrees well with the global maximum condition, $a_1 = a_2 = \dots = a_i = \dots = a_n$, predicted by the equality condition of the Cauchy–Schwarz inequality in the continuum limit.

These results indicate that the optimized packaging ratio η_{opt} increases as the number of cells n increases, as predicted by equation (8) and validated by Fig. 4c. This implies that a sufficiently high packaging ratio can be achieved simply by increasing the number of cells in the origami layout. Additionally, as seen from equation (8), the optimized packaging ratio η_{opt} increases linearly with the number of cells n , and the slope depends solely on the target shape. This slope can be interpreted as the per-cell packaging efficiency, which quantifies how much the packaging ratio increases per additional cell for a given geometry. Fig. 4d shows how the per-cell packaging efficiency varies for the superellipses defined by $x = \text{sgn}(\cos \theta)|\cos \theta|^{2/m}$ and $y = \gamma \text{sgn}(\sin \theta)|\sin \theta|^{2/m}$. As shown in Fig. 4d, the per-cell packaging efficiency increases as the cross-section of the target shape becomes more polygonal, whereas it decreases as the target shape becomes increasingly anisotropic. This result implies that the per-cell packaging efficiency increases as the target shape becomes overall flatter, since the flat-foldable constraint equations (1) and (2) allow for a reduction in the panel thickness. Additionally, an anisotropic target shape—which generates a greater number of asymmetric cells under the flat-foldable constraint equation (3)—implies a lower per-cell packaging efficiency.

2.4 Deployable origami wing and flight test

The engineering applicability of the proposed origami design method was demonstrated through a successful flight test of a deployable origami wing designed with this method (Fig. 5 and Supplementary Movie 2). An aircraft wing was selected as the demonstration platform for two main reasons. First, the wing serves as an excellent platform for verifying the geometric fidelity of the proposed origami structure. This is because the aerodynamic performance of a wing critically depends on having a precisely defined airfoil shape, thereby demanding accurate airfoil reproduction. Second, the wing must retain its shape under aerodynamic loading during flight, making it a stringent test case for verifying the structural stability of the design. Moreover, since aerodynamic loading scales with the overall weight of the aircraft, this test provides a validation of the intrinsic structural robustness of our method that is independent of the choice of material.

The origami wing was designed to have a NACA 2412 airfoil when fully deployed, as shown in Fig. 5a, with two vertical spars incorporated to withstand the bending moment generated by aerodynamic lift. As shown in Fig. 5b, the structure is capable of flat-folding. In addition, since it has flat regions on its outer surfaces in the flat-folded configuration, the wing can be further compactly stowed by spanwise zig-zag folding using simple piano hinges. During spanwise deployment, the spars were connected through interference fits. Subsequently, the unbonded interfaces were secured with neodymium magnets to maintain the structure in the deployed configuration. Fig. 5c shows the deployable origami wing in both the stowed and deployed configurations on the fabricated UAV. When stowed, the wing volume is reduced by approximately 53%, and the span is further reduced to one-third of its original length through two spanwise foldings. The folding motion of the origami wing can be found in Supplementary Movie 2.

The demonstrator aircraft was designed around an already-fabricated foldable-wing prototype. Because this prototype wing weighed approximately 500 g—significantly heavier than a conventionally built fixed wing—the mass of the remaining airframe components was minimized to keep the overall takeoff weight comparable to other unmanned aircraft of similar size. Since ailerons could not be installed on the foldable wing, center wing mounts were fabricated to provide a 10° dihedral angle for roll stability. These mounts also carried the bending loads through a carbon-fiber tube that passed through the upper main spar. Incorporating the center mounts increased the total wingspan by 60 mm. The aircraft was aerodynamically designed using AVL [35], and the resulting specifications are summarized in Table 1. The drag of the wing and horizontal tail was estimated as a function of the lift coefficient C_L by inferring sectional drag coefficients C_d from two-dimensional airfoil data—NACA 2412 for the wing and a flat-plate model for the tail. The drags of the fuselage and vertical stabilizer were estimated using skin-friction coefficients and standard form factors. Equation (9) represents the drag polar.

$$C_D = 0.029 + 0.072(C_L - 0.034)^2 \quad (9)$$

The motor and propeller were selected based on the electric-propulsion system analysis presented in [36].

The UAV was designed to be remotely controlled from the ground (Supplementary Note 5) and successfully demonstrated stable flight for approximately 20 seconds, including altitude adjustments and turning maneuvers (Fig. 5d and Supplementary Movie 2). This indicates that our origami wing, designed to target the NACA 2412 airfoil, generated sufficient lift through accurate airfoil reproduction while remaining structurally stable. In particular, as shown in Supplementary Movie 2, it was confirmed that

the deployed configuration could be stabilized under aerodynamic load simply by securing the unbonded interfaces with magnets.

3 Discussion

We propose an inverse design method for constructing a flat-foldable thick origami structure with a smooth curved outer surface. Here, we introduce the flat-foldable constraints in their Euclidean geometric form (for generalized cylinders) and extend them to their spherical geometric form (for generalized cones). Additionally, for generalized cylinders, we revealed that the optimized packaging ratio increases without bound as the number of cells increases, and that the per-cell packaging efficiency depends on the target shape. We demonstrated that our proposed structure is sufficiently stable under loading conditions by fabricating a deployable origami wing and conducting a successful flight test. Several recent studies [28,30] have also explored origami concepts featuring smooth curved surfaces. However, their approaches are based on embedding origami patterns defined as tessellations (e.g., Miura-ori, flasher) onto curved surfaces, and their demonstrations are limited to finite, disk-like surfaces (e.g., paraboloid and parabolic cylindrical surface). By contrast, our methodology does not rely on tessellation-defined origami patterns and applies to topologically annular surfaces, specifically generalized cylinders and generalized cones. This capability unlocks practically important applications that are not disk-like, including aircraft wings and helical antennas. Furthermore, unlike prior studies, we demonstrated that our proposed structure, upon deployment, maintains sufficient structural stability under loading conditions. Our methodology is broadly applicable to developable surfaces, but—because it assumes straight crease lines—it does not readily extend to doubly curved surfaces.

Our methodology mitigates packaging constraints in domains where curved surface geometry is critical—such as aerospace and communications—thereby enabling improved performance and greater design freedom. In aerospace, systems that must operate in constrained urban environments—such as UAM vehicles—and man-portable UAVs could carry larger wings, thereby achieving improved flight performance. Furthermore, aircraft-type planetary probes [18,19] can be packaged within tight rocket fairings even with larger wings, enabling delivery to the destination; the resulting gains in flight performance translate into improved exploration performance, with greater payload capacity for scientific instruments and broader coverage. For electromagnetic communications, our method enables helical and conical antennas to be stowed, markedly easing antenna-size limitations in volume-constrained platforms (e.g., CubeSats) and, in turn, broadening the usable frequency spectrum.

4 Methods

4.1 Prototype and Origami Wing Fabrication

The prototypes in Fig. 3 were fabricated using a fused deposition modeling (FDM) 3D printer (Prusa MK4, Prusa Research) with polylactic acid (PLA) filament (PLA-Basic filament, eSUN). The origami wing shown in Fig. 5 was 3D printed using a lightweight polylactic acid (PLA) filament (ePLA-LW filament, eSUN). The creases were fabricated using either a polyethylene terephthalate (PET) sheet of 0.2mm thickness or polyester film (Oracover, Lanitz-Prena Folien Factory GmbH), which were bonded to the 3D printed panels with an ethyl cyanoacrylate adhesive (Loctite 401, Henkel).

References

- [1] Jamalimehr, A., Mirzajanzadeh, M., Akbarzadeh, A. & Pasini, D. Rigidly flat-foldable class of lockable origami-inspired metamaterials with topological stiff states. *Nat. Commun.* **13**, 1–14 (2022).
- [2] Silverberg, J. L. et al. Using origami design principles to fold reprogrammable mechanical metamaterials. *Science* **345**, 647–650 (2014).
- [3] Zhao T. et al. Modular chiral origami metamaterials. *Nature* **640**, 931–940 (2025).
- [4] Fang, H., Chu, S. C. A., Xia, Y., & Wang, K. W. Programmable Self-Locking Origami Mechanical Metamaterials. *Adv. Mater.* **30**, 1706311 (2018).
- [5] Yasuda, H. et al. Origami-based impact mitigation via rarefaction solitary wave creation. *Sci. Adv.* **5**, eaau2835 (2019).

- [6] Kim, S.-J., Lee, D.-Y., Jung, G.-P. & Cho, K.-J. An origami-inspired, self-locking robotic arm that can be folded flat. *Sci. Robot.* **3**, eaar2915 (2018).
- [7] Ze, Q. et al. Soft robotic origami crawler. *Sci. Adv.* **8**, eabm7834 (2022).
- [8] Felton, S., Tolley, M., Demaine, E., Rus, D. & Wood, R. A method for building self-folding machines. *Science* **345**, 644–646 (2014).
- [9] Melancon, D., Gorissen, B., García-Mora, C. J., Hoberman, C. & Bertoldi, K. Multistable inflatable origami structures at the metre scale. *Nature* **592**, 545–550 (2021).
- [10] Zhu, Y. & Filipov, E. T. Large-scale modular and uniformly thick origami-inspired adaptable and load-carrying structures. *Nat. Commun.* **15**, 2353 (2024).
- [11] Peng, R., & Chirikjian, G. S. Thick-panel origami structures forming seamless surfaces. *Nat. Commun.* **16**, 3881 (2025).
- [12] Miura, K. Method of packaging and deployment of large membranes in space. *Inst. Space Astronaut. Sci. Rep.* **618**, 1–9 (1985).
- [13] Zirbel, S. A. et al. Accommodating thickness in origami-based deployable arrays. *J. Mech. Des.* **135**, 111005 (2013).
- [14] Zhao, J.-S., Chu, F. & Feng, Z.-J. The mechanism theory and application of deployable structures based on SLE. *Mech. Mach. Theory* **44**, 324–335 (2009).
- [15] Mira, L. A., Thrall, A. P. & De Temmerman, N. Deployable scissor arch for transitional shelters. *Autom. Constr.* **43**, 123–131 (2014).
- [16] Siéfert, E., Reyssat, E., Bico, J. & Roman, B. Bio-inspired pneumatic shape-morphing elastomers. *Nat. Mater.* **18**, 16692–16696 (2019).
- [17] Usevitch, N. S. et al. An untethered isoperimetric soft robot. *Sci. Robot.* **5**, eaaz0492 (2020).
- [18] Johnson, W. et al. *Mars Science Helicopter Conceptual Design*. NASA Technical Memorandum NASA/TM-2020-220485 (NASA Ames Research Center, 2020).
- [19] Fujita, K., Luong, R., Nagai, H. & Asai, K. Conceptual design of Mars airplane. *Trans. Jpn. Soc. Aeronaut. Space Sci.* **10**, Te_5–Te_10 (2012).
- [20] Amend, C., Nurnberger, M., Oppenheimer, P., Koss, S. & Purdy, B. A Novel Approach for a Low-Cost Deployable Antenna. In *40th Aerospace Mechanisms Symposium* 12-14 (The Aerospace Mechanisms Symposium (AMS), Cocoa Beach, FL, 2010).
- [21] Dudte, L. H., Vouga, E., Tachi, T. & Mahadevan, L. Programming curvature using origami tessellations. *Nat. Mater.* **15**, 583–588 (2016).
- [22] Hu, Y., Zhou, Y. & Liang, H. Constructing rigid-foldable generalized Miura-ori tessellations for curved surfaces. *J. Mech. Rob.* **13**, 011017 (2021).
- [23] Wang, F., Gong, H., Chen, X. & Chen, C. Q. Folding to curved surfaces: A generalized design method and mechanics of origami-based cylindrical structures. *Sci. Rep.* **6**, 33312 (2016).
- [24] Wang, S., Wu, J., Yan, P., Huang, H., Li, B. & Liu, R. Design of deployable circular structures based on Miura origami pattern. *Mech. Mach. Theory* **186**, 105350 (2023).
- [25] Tachi, T. Designing freeform origami tessellations by generalizing Resch’s patterns. *J. Mech. Des.* **135**, 111006 (2013).
- [26] Yu, Y., Chen, Y. & Paulino, G. Programming curvatures by unfolding of the triangular Resch pattern. *Int. J. Mech. Sci.* **238**, 107861 (2023).
- [27] Wang, S., Gao, Y., Huang, H., Li, B., Guo, H. & Liu, R. Design of deployable curved-surface rigid origami flashers. *Mech. Mach. Theory* **167**, 104512 (2022).

- [28] Tian, D., Yang, X., Jin, L., Shi, Z., Guo, H. & Liu, R. Design and analysis of a solid surface deployable antenna mechanism based on flasher rigid origami. *Thin-Walled Struct.* **201**, 112033 (2024).
- [29] Yao, S., Zekios, C. L. & Georgakopoulos, S. V. A rigidly foldable and reconfigurable thick origami antenna. *Philos. Trans. R. Soc. A* **382**, 20240002 (2024).
- [30] Zhang, Y., Li, M., Chen, Y., Peng, R. & Zhang, X. Thick-panel origami-based parabolic cylindrical antenna. *Mech. Mach. Theory* **182**, 105233 (2023).
- [31] Wang, C., Guo, H., Liu, R. & Deng, Z. A programmable origami-inspired space deployable structure with curved surfaces. *Eng. Struct.* **256**, 113934 (2022).
- [32] McKay, B. D. Isomorph-Free Exhaustive Generation. *J. Algorithms* **26**, 306–324 (1998).
- [33] Miura, K. & Pellegrino, S. *Forms and Concepts for Lightweight Structures* Cambridge Univ. Press, (2020).
- [34] Bortolotti, P., Johnson, N., Abbas, N. J., Anderson, E., Camarena, E. & Paquette, J. Land-based wind turbines with flexible rail-transportable blades. Part I: Conceptual design and aeroservoelastic performance. *Wind Energy Sci.* **6**, 1277–1290 (2021).
- [35] Drela, M., & Youngren, H. (n.d.). AVL (Athena Vortex Lattice): Subsonic lifting-line theory aircraft design and analysis code. Massachusetts Institute of Technology. Retrieved from <http://web.mit.edu/drela/Public/web/avl/>.
- [36] Nam, H., Lee, S. & Lee, H. Electric propulsion system analysis using performance maps. *IEEE Trans. Aerosp. Electron. Syst.* **61**, 8476–8489 (2025).

Table 1: Aircraft specifications.

Takeoff mass	850 g
Wingspan	1.26 m
Wing area	0.315 m ²
Cruise speed	8.5 m/s
Cruise C_L	0.65
Static margin	8-10%
Motor	T-Motor AS2304 KV1800
Propeller diameter	8 inch
Electric propulsion system efficiency	45%
Estimated flight time	9 minutes

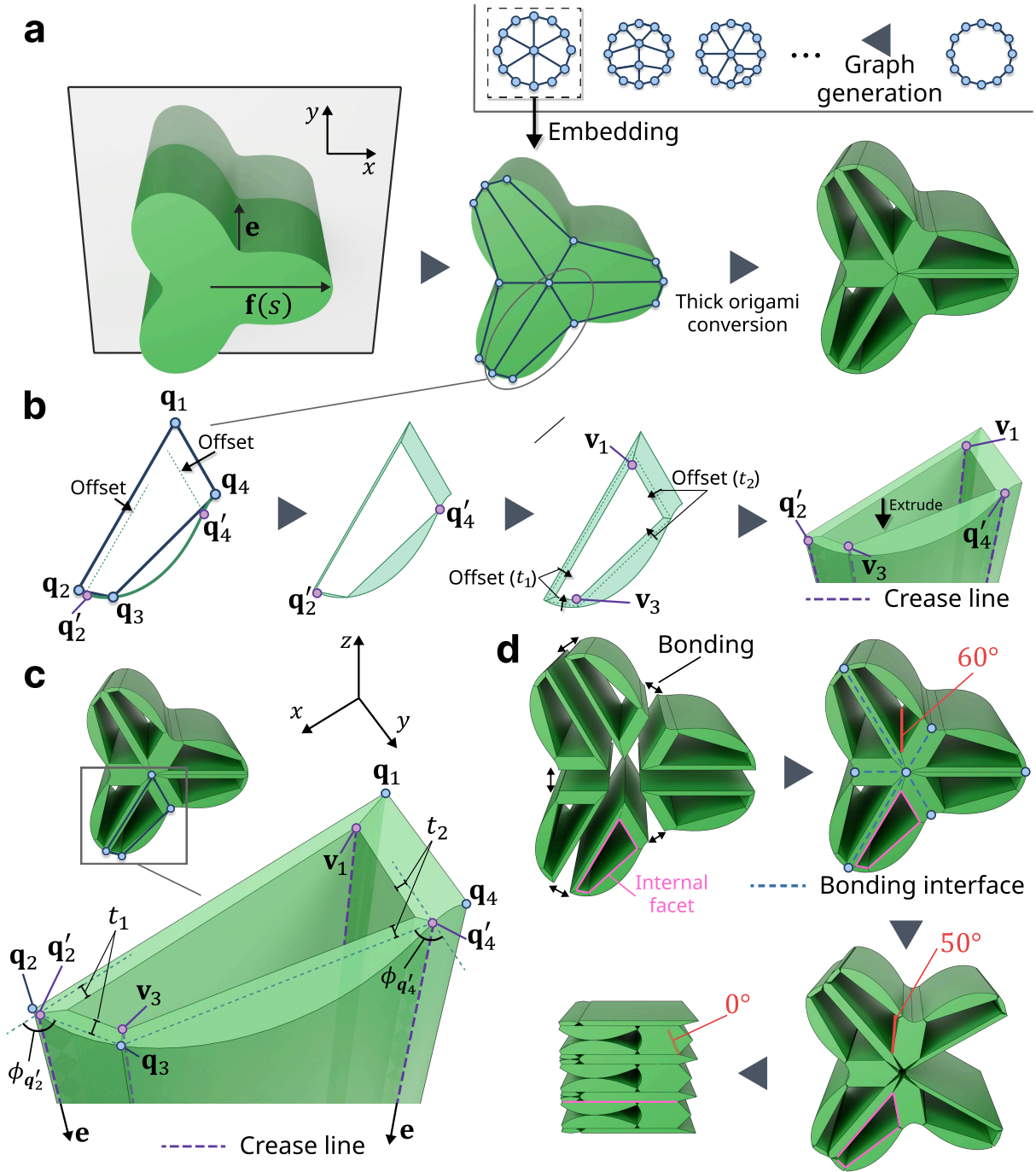


Figure 1: **Flat-foldable thick origami structure for generalized cylinders.** **a** Overall process of converting a generalized cylinder into a flat-foldable thick origami. The design process is performed on a plane perpendicular to the vector \mathbf{e} , shown as the gray plane (xy -plane). **b** Construction process of a flat-foldable thick origami cell. **c** Geometry of a flat-foldable thick origami cell. Blue points ($\mathbf{q}_1, \mathbf{q}_2, \mathbf{q}_3, \mathbf{q}_4$) denote vertices of the embedded graph, and magenta points ($\mathbf{q}'_2, \mathbf{q}'_4, \mathbf{v}_1, \mathbf{v}_3$) together with dashed lines indicate creases. All vectors lie on the xy -plane. **d** Construction of the thick origami structure and its flat-folding sequence. Blue dashed lines indicate bonding interfaces, which correspond to internal edges, and the red solid line denotes the \mathbf{v}_1 crease of a representative cell. Magenta regions indicate internal facets that become coplanar in the flat-folded configuration.

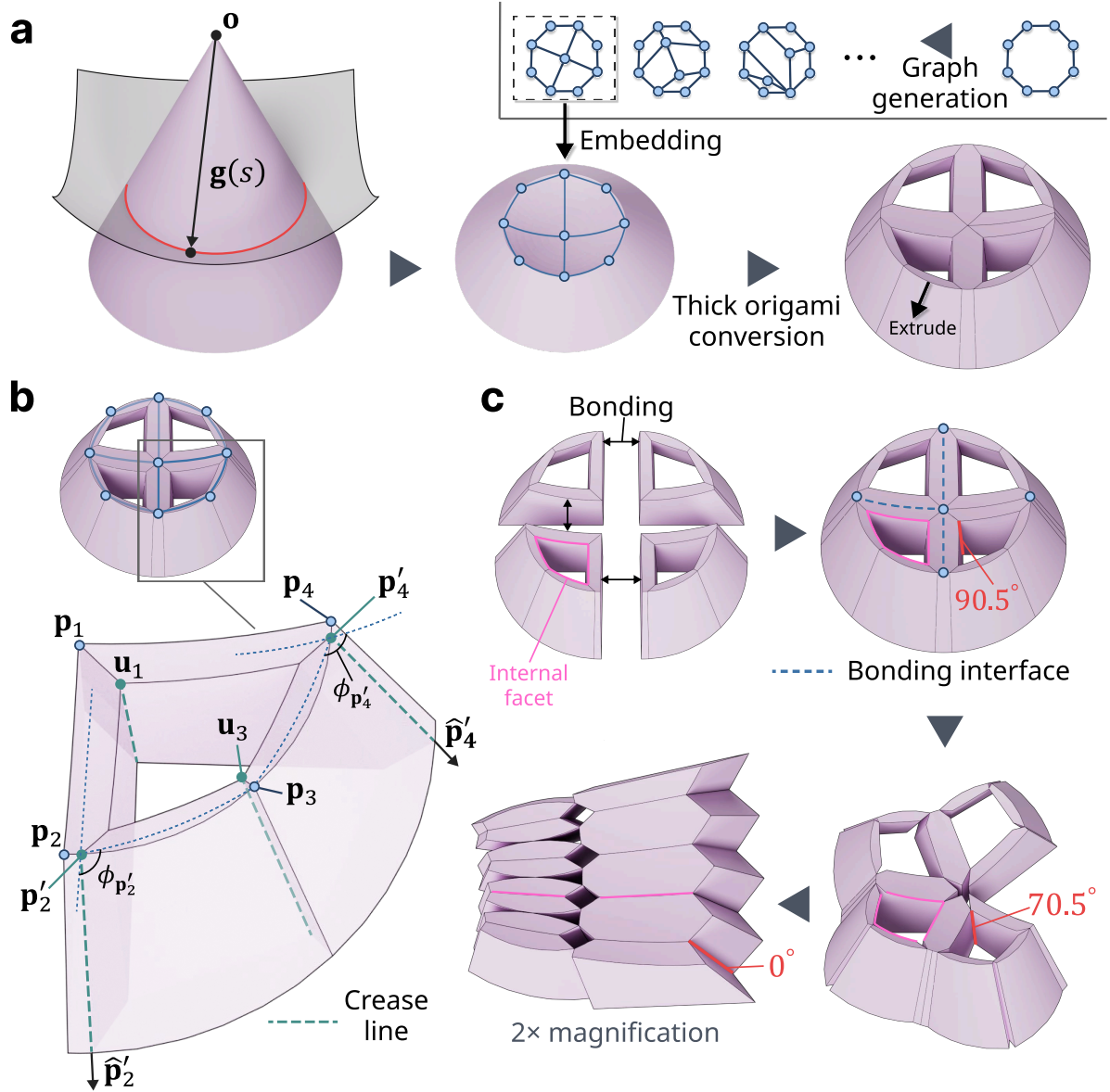


Figure 2: **Flat-foldable thick origami structure for generalized cones.** **a** Overall process of converting a generalized cone into a flat-foldable thick origami. The design process is performed on a unit sphere centered at the point \mathbf{o} , shown as the gray plane. **b** Geometry of a flat-foldable thick origami cell. Blue points ($\mathbf{p}_1, \mathbf{p}_2, \mathbf{p}_3, \mathbf{p}_4$) denote vertices of the embedded graph, while teal points ($\mathbf{p}'_2, \mathbf{p}'_4, \mathbf{u}_1, \mathbf{u}_3$) and dashed lines indicate creases. **c** Construction of the thick origami structure and its flat-folding sequence. Blue dashed lines indicate bonding interfaces, which correspond to internal edges, and the red solid line denotes the \mathbf{u}_1 crease of a representative cell.

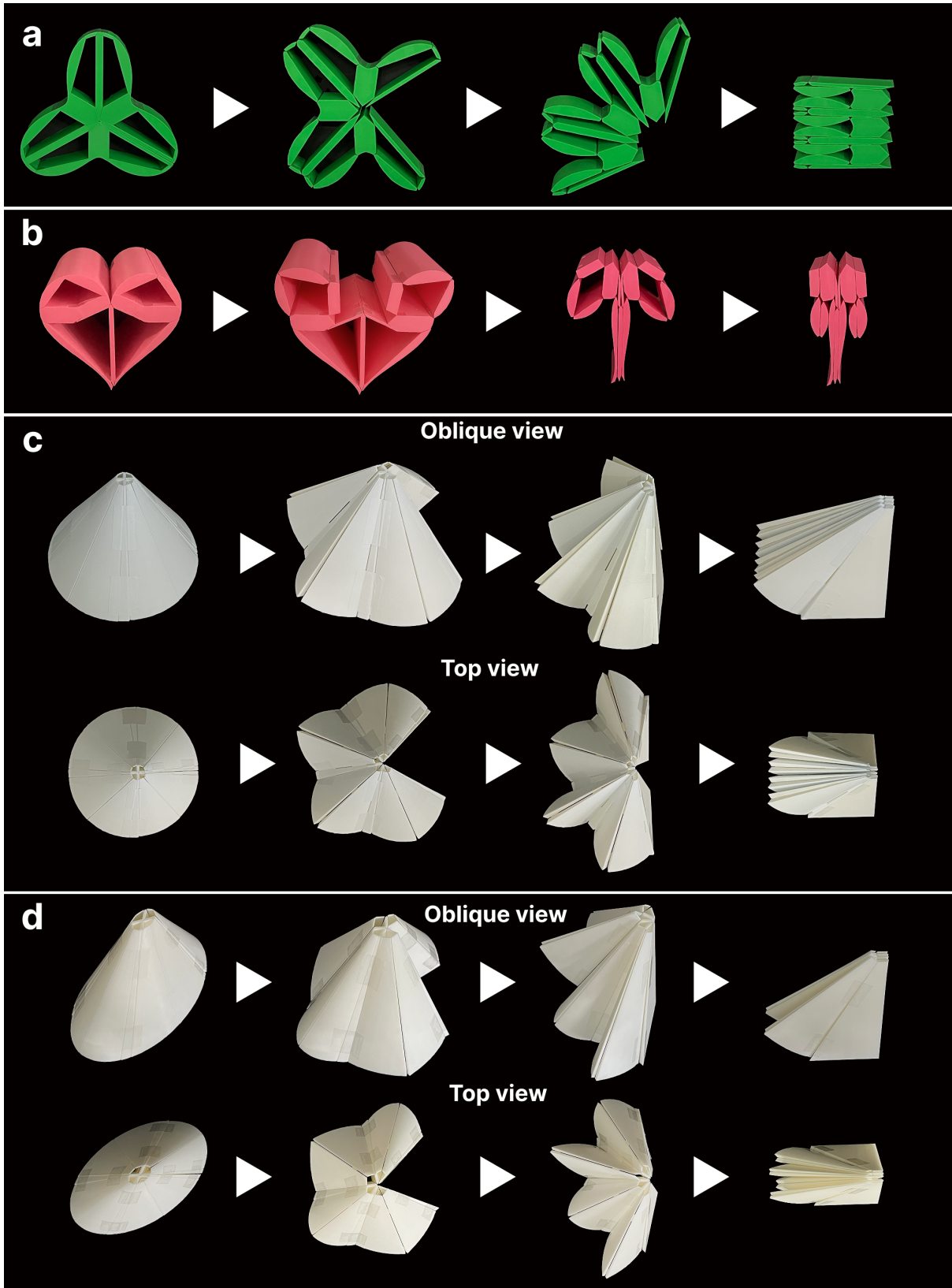


Figure 3: **Flat-foldable thick origami prototypes for various generalized cylinders and generalized cones.** **a** Generalized cylinder with a three-leaf-clover-shaped cross-section. **b** Generalized cylinder with a heart-shaped cross-section. **c** Generalized cone with a circular cross-section (cone). **d** Generalized cone with an elliptical cross-section (elliptic cone).

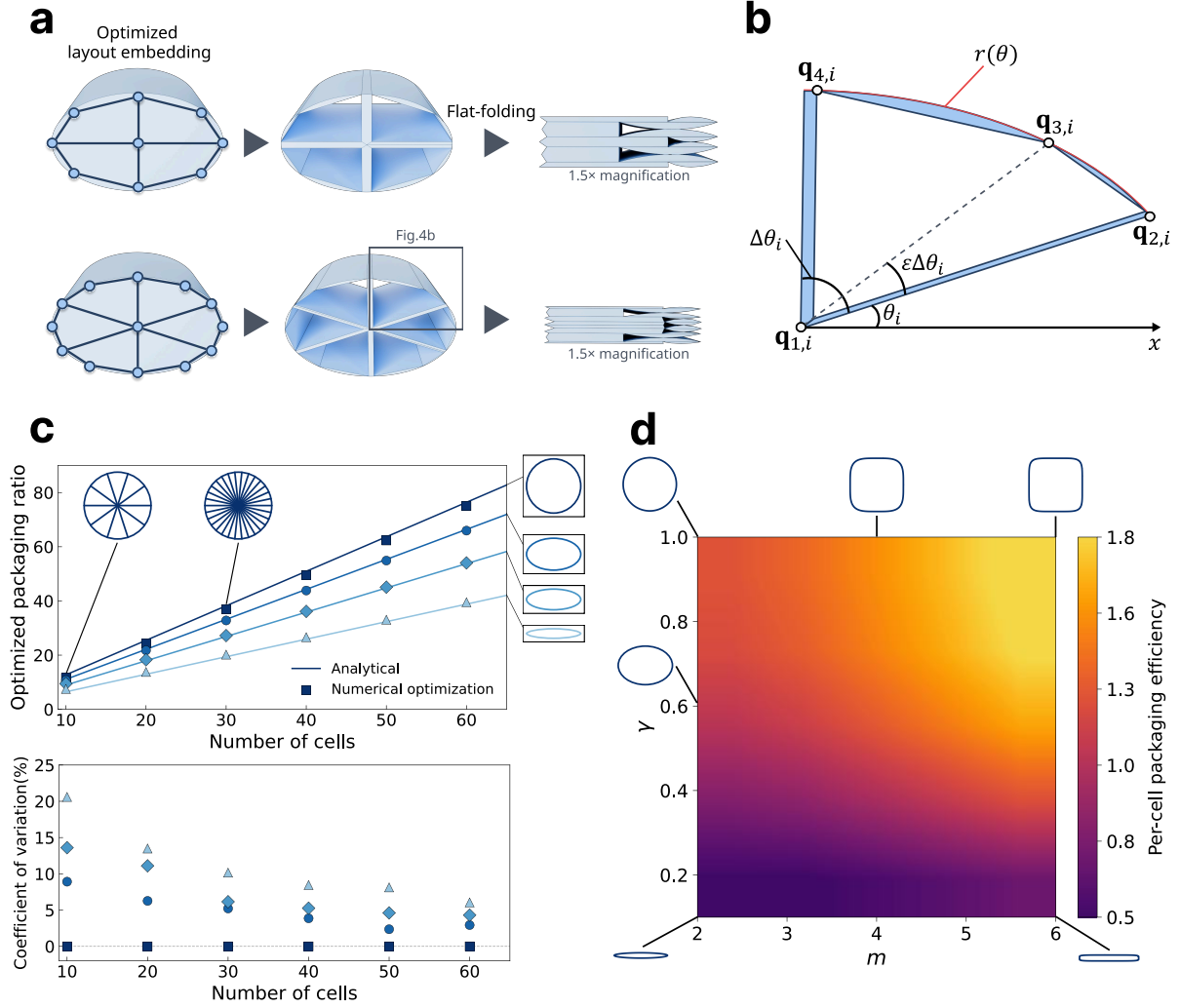


Figure 4: **Relationship between optimal packaging ratio and the number of cells.** **a** Conversion of a generalized cylinder with an elliptical cross-section (eccentricity 0.8) into flat-foldable thick origami structures based on graphs with 4 and 6 internal faces (4-cell and 6-cell cases). The positions of graph vertices are numerically optimized during graph embedding to achieve higher packaging ratios, yielding values of 4.2 and 6.4, respectively. **b** Geometry of the i -th thick origami cell in cross-section. The cross-sectional outline of the generalized cylinder (target shape) is highlighted in red. **c** (top) Plot of the optimized packaging ratio versus the number of cells n for a generalized cylinder with an elliptical cross-section. Results are shown for elliptical aspect ratios of 1.0, 0.6, 0.4, and 0.2. The solid lines represent the analytical continuum-limit expression of the optimal packaging ratio, while the markers indicate local maxima obtained through numerical optimization. (bottom) Plot of the coefficient of variation of the origami cell areas $\{a_1, a_2, \dots, a_n\}$ obtained from each numerical optimization. **d** Heatmap of the analytically obtained per-cell packaging efficiency for superellipses defined as $x = \text{sgn}(\cos \theta)|\cos \theta|^{2/m}$ and $y = \gamma \text{sgn}(\sin \theta)|\sin \theta|^{2/m}$.

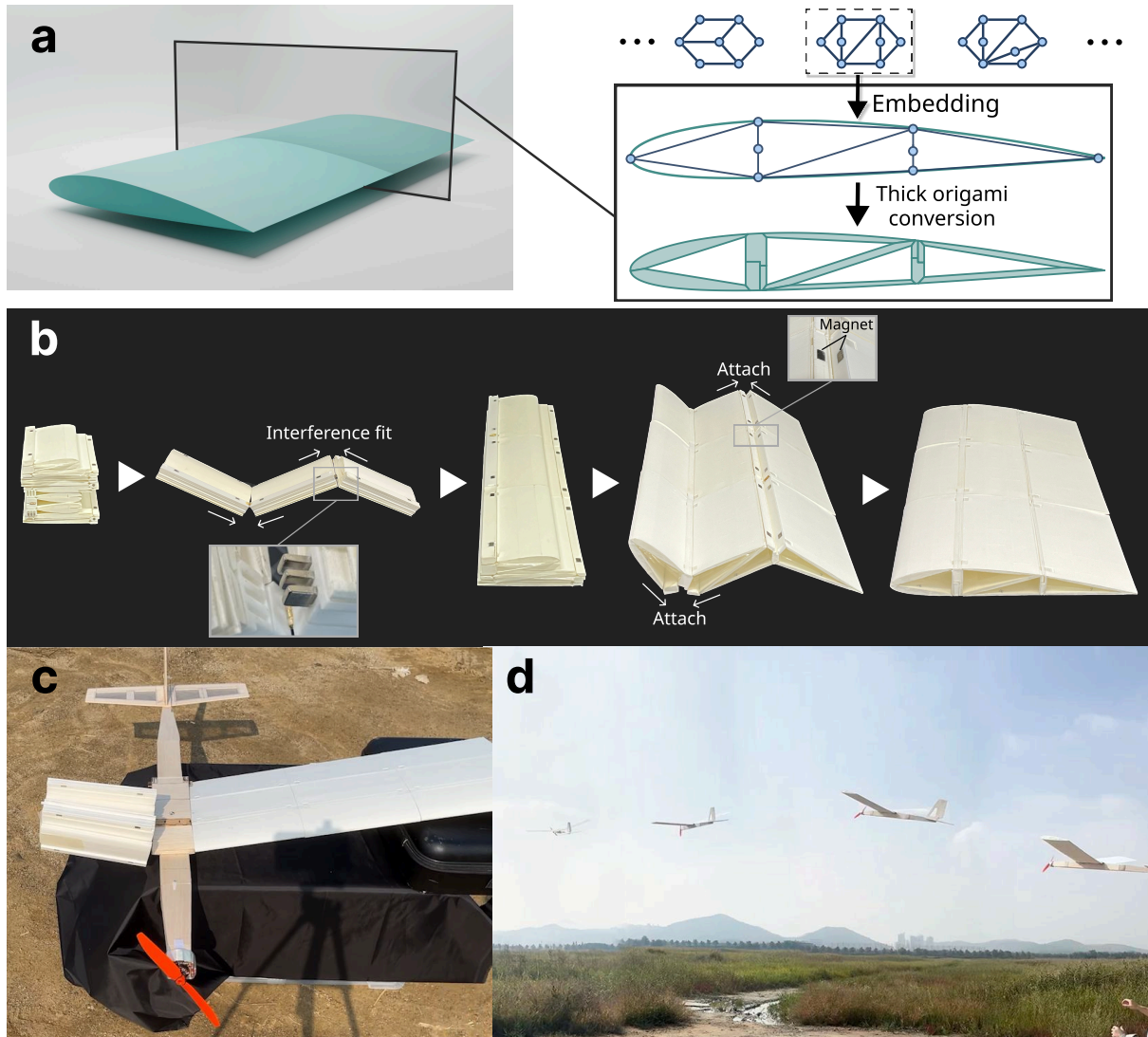


Figure 5: **Design and flight test of a deployable origami wing.** **a** Process of converting an aircraft wing with a NACA 2412 airfoil into a flat-foldable thick origami. The origami layout is deliberately selected and embedded to incorporate two vertical spars within the structure. **b** Deployment sequence of the origami wing. The first three stages show the spanwise folding process in reverse, while the final two stages represent the reverse of flat-folding. **c** Prototype UAV equipped with the deployable origami wing. The left wing is stowed, while the right wing is fully deployed for flight testing. **d** Flight trajectory of the UAV equipped with the deployable origami wing during flight testing.